

## Article

# Study of Self-Excited Thermomechanical Oscillator with Shape Memory Alloys

Ivo Yotov<sup>1</sup>, Georgi Todorov<sup>2</sup> and Todor Todorov<sup>1,\*</sup> 

<sup>1</sup> Department of Theory of Mechanisms and Machines, Faculty of Industrial Technology, Technical University of Sofia, 1797 Sofia, Bulgaria; ivyotov@tu-sofia.bg

<sup>2</sup> Department of Manufacturing Technology and Systems, Technical University of Sofia, 1797 Sofia, Bulgaria; gdt@tu-sofia.bg

\* Correspondence: tst@tu-sofia.bg

**Abstract:** In this paper, a new type of self-excited thermomechanical oscillator containing an oscillating shape memory alloy (SMA) filament with two symmetrically arranged spheres is investigated. The self-excitation of the oscillations is due to a heater of constant temperature, which causes periodic contractions of the filament when it approaches it. The contracted filament moves away from the heater a distance sufficient to cool it. Under the action of the weight of the spheres, the cooled filament re-approaches the heater, causing the above processes to repeat periodically. On the basis of experimental studies, approximating functions of the heater's heat field distribution are derived. A dynamic model of the oscillator has been created, in which the minor and major hysteresis in the SMA alloy and the distribution of the heat field around the heater have been taken into account. Through numerical solutions of the differential equations, the laws of motion of the spheres are obtained. The displacements of the spheres in two perpendicular directions were measured using an experimental system. The obtained experimental results validate the proposed dynamic model and its assumptions with a high degree of confidence. Conclusions are drawn about the stochastic nature of the oscillations due to the hysteresis properties of the SMA and the temperature variation of the natural frequency of the oscillating system.

**Keywords:** self-excited oscillations; vibrations; shape memory alloy; thermomechanical oscillations



**Citation:** Yotov, I.; Todorov, G.; Todorov, T. Study of Self-Excited Thermomechanical Oscillator with Shape Memory Alloys. *Actuators* **2024**, *13*, 182. <https://doi.org/10.3390/act13050182>

Academic Editors: Luis Enrique Moreno Lorente, Maria Dolores Blanco Rojas and Dorin Sabin Copaci

Received: 8 April 2024  
Revised: 7 May 2024  
Accepted: 9 May 2024  
Published: 11 May 2024



**Copyright:** © 2024 by the authors. Licensee MDPI, Basel, Switzerland. This article is an open access article distributed under the terms and conditions of the Creative Commons Attribution (CC BY) license (<https://creativecommons.org/licenses/by/4.0/>).

## 1. Introduction

Self-excited oscillations accompany many technological processes and, in most cases, have detrimental effects on them. The main reasons for their occurrence are mainly the dependence of friction forces on relative sliding, changes of normal loads, viscoelastic interactions, or the influence of various geometrical effects [1–3].

It has been shown that purely temperature-focussed self-excited oscillations cannot exist because the heat conduction equation, unlike other equations of mechanics, is not invariant under time reversal. Periodic thermally forced self-excited oscillations that propagate as waves are possible [4]. The combination of thermal and mechanical vibrations is known by the term thermomechanical oscillations (TMO). The foundations of the theory of TMOs were laid in 1829 by A. Travelian [5] and were later further developed by M. Faraday, A. Tyndal, and J. Rayleigh. Some of the first theoretical and experimental studies of the conditions for the occurrence of self-excited thermomechanical oscillations were reported by Nesis E. I. [4]. Awrejcewicz and Pyryev [6] created a massless elastic element model of frictional self-excited vibrations and investigated the possibilities of their existence.

Thermomechanical self-excited oscillations have a negative influence on many technological processes. To show that the loss of stability in constant speed cutting is due to thermomechanical self-excited oscillations, authors Astashev and Korendyasev [7] investigated the model of heat generation in the cutting region. Fel'dshtein [8] investigated

self-excited thermomechanical oscillations of current-carrying wires by determining the existence conditions and describing them by numerical simulations. Toda et al. [9], using the Barenblatt model, investigated the thermomechanical self-excited oscillations that occur during cold drawing of films. A technique to stabilize and suppress the oscillations in an optothermomechanical oscillator is demonstrated in [10].

In microelectromechanical systems (MEMS), thermal processes occur at a much higher rate than in conventional macrosystems due to the significantly lower values of temperature and time constants. And in these systems, one can note detrimental effects of self-excited thermomechanical oscillations, such as those induced by laser heating of double-clamped MEMS beams [11], or the induced frequency self-locking that occurs when laser illuminating thin MEMS resonators [12,13].

The micrometric dimensions of thermally exposed components in MEMS create conditions for building fundamentally new devices in which self-excited thermomechanical oscillations are the basis of their operating principle. One such large class of MEMS are self-excited thermomechanical microresonators [14,15], which are in competition with their capacitive [16] and piezoelectric analogues [17].

Shape memory alloys (SMAs) are smart materials possessing the property of remembering a shape, which, if changed within certain limits, can be fully recovered by heating. When the change of the shape is brought about by stretching due to tensile stress, the SMA specimen tends to shorten to its original undeformed dimensions when it is restored. This behavior is used to create relatively low-cost actuators that possess several advantages, such as generating large forces and displacements at high energy density and noiselessness. Thermal activation of SMAs creates conditions for cyclic control [18–20] and, in many cases for self-excitation, of thermomechanical oscillations [21–24]. In their low-temperature state, SMAs have a martensitic crystallographic structure which is soft and deformable. Martensite has two crystallographic forms: a twinned and a detwinned form. Undeformed martensite is called twinned, and it preserves the set shape. When deformed, martensite changes to its detwinned crystallographic form, achieving a large strain in the order of 8%. Once heated, the SMA transforms into the austenitic state where the memorized shape is recovered. The crystallographic transformation temperatures depend on their chemical composition and can be tailored over a wide range.

Oscillating systems based on shape memory alloys are widely used in energy harvesting technologies. Several researchers use SMA substrates on which they deposit a piezoelectric layer to generate electricity by vibration [25–28]. Another interesting application of SMAs in energy harvesting systems is the two-step conversion of heat to mechanical and then mechanical to electrical energy [29–31]. A peculiarity of thermomechanical models with SMAs are the nonlinearities arising from the hysteresis in the stress–strain, stress–temperature, and temperature–strain relationships. The existence conditions of oscillatory modes of nonlinear thermomechanical self-excited systems with hysteresis are a challenge for modern research in the field of differential equations and control theory [22,32].

The most popular methods for self-excitation of SMAs are via the Joule effect, i.e., heating with an eclectic current [33]; via convection using heaters [29]; and radiatively, for example, via solar energy [34].

The aim of this paper is to create a mathematical model of a new self-excited thermomechanical oscillator with SMA filament, to validate the obtained results experimentally, and to draw conclusions about the type and parameters of oscillations. In the development of the mathematical model, the aim is to describe the thermodynamic processes in detail, considering the hysteresis phenomena in the SMA filament.

## 2. Design Concept of the Self-Excited Thermomechanical Oscillator

The schematic of the self-excited thermomechanical oscillator is shown in Figure 1. The structure is symmetrical consisting of an SMA filament  $OABC$ , rigidly fixed at both ends, on which two metal spheres in points A and B are arranged. Nitinol (NiTi) SMA was

used for the filament [33]. A heater is fixedly located at the base of the thermomechanical oscillator. At room temperature ( $T_0 = 20\text{ }^\circ\text{C}$ ), the SMA filament is in a martensitic state.

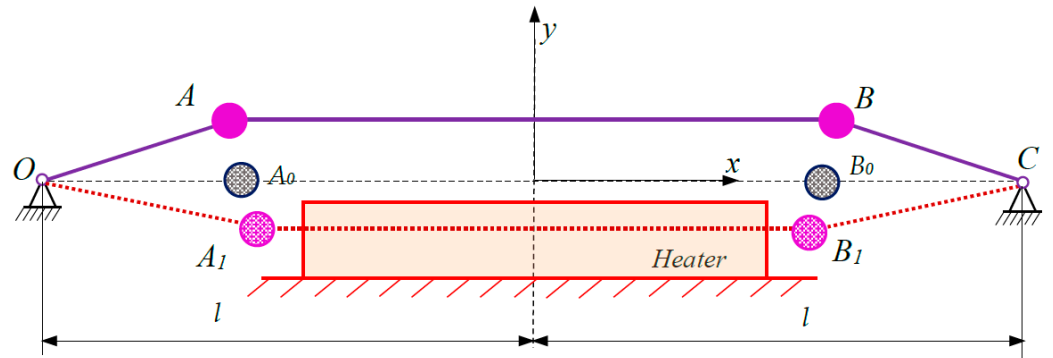


**Figure 1.** Scheme of the self-exciting thermomechanical oscillator.

The principle of the oscillator is as follows: Under the action of the weight of the two spheres, the SMA filament sags and approaches the heater at position  $OA_1B_1C$ . The proximity of the filament to the heater raises its temperature and causes contraction while, at the same time, hardening it. The contracted filament rises back vertically under the temperature, moving away from the heater at position  $OA_0B_0C$ . This is followed by a lowering of the temperature and a softening and relaxation of the filament. As a result, under the weight of the spheres, the filament falls again and approaches the heater at position  $OA_1B_1C$ . This is followed by a cyclic repetition of the above processes, resulting in periodic oscillations of the system.

### 3. Building a Dynamic Model and Determining the Input Data for Its Solution

The SMA filament in the static position is pre-stretched between the  $OC$  supports. The distance between the supports is assumed to be  $OC = 2l$ , and the half-length of filament before tensioning is  $l_s$ . Thus, for half of the prestrain of the SMA filament,  $\Delta l_{s0}$  is valid:

$$\Delta l_{s0} = l - l_s. \tag{1}$$

The  $x$ -axis of the coordinate system  $Oxy$  is chosen to lie on the segment  $OC$ , and its origin is located in the middle of the same segment. Symmetrically to the  $y$ -axis on the  $OC$  segment, two points,  $A_0$  and  $B_0$ , are selected, at which two spheres of equal mass ( $m$ ) are fixed. The distances along the horizontal  $x$ -axis are denoted by  $l_{10} = OA_0$ ,  $l_{20} = A_0B_0$ , and  $l_{30} = B_0C$ . Since for the relative lengths, the notations

$$\frac{l_{01}}{l} = \frac{l_{03}}{l} = \lambda_0, \tag{2}$$

are chosen; then, for the deformations from the prestressing,  $\Delta l_{s10}$  and  $\Delta l_{s30}$  in the end sections  $OA_0$  and  $B_0C$  will follow:

$$\Delta l_{s01} = \Delta l_{s03} = \Delta l_{s0}\lambda_0, \tag{3}$$

and in the middle section ( $A_0B_0$ ), this deformation will be

$$\Delta l_{s012} = 2\Delta l_{s0}(1 - \lambda_0). \tag{4}$$

It can be seen in Figure 1 that due to the symmetrical arrangement of the heater and the SMA filament, only the middle section of the  $AB$  will be heated. It is assumed that the temperature of this section is distributed uniformly along its length.

Since the dynamic model will be constructed using the Lagrange equations of the second kind, the kinetic energy of the oscillator is represented in the following form:

$$E_k = \frac{m}{2} (\dot{x}_A^2 + \dot{x}_B^2 + \dot{y}_A^2 + \dot{y}_B^2), \quad (5)$$

where  $\dot{x}_A$ ,  $\dot{x}_B$  are the velocities of points A and B on the x-axis, and  $\dot{y}_A$ ,  $\dot{y}_B$  are the velocities of points A and B on the y-axis.

The end sections OA and BC are assumed not to heat up, unlike the middle AB section, which changes its temperature and Young's modulus, so the potential energy takes the following expression:

$$E_p = \frac{k_l}{2} (\Delta l_1^2 + \Delta l_3^2) + \frac{k_T}{2} \Delta l_2^2, \quad (6)$$

where  $k_l$  is the elastic constant of the extreme cold sections,  $k_T$  is the elastic constant of the middle warm section,

$$\Delta l_1 = \sqrt{(x_A - x_O)^2 + (y_A - y_O)^2} - l_{10} + \Delta l_{s0} \lambda_0 \quad (7)$$

$$\Delta l_3 = \sqrt{(x_B - x_C)^2 + (y_B - y_C)^2} - l_{30} + \Delta l_{s0} \lambda_0 \quad (8)$$

are the deformations of the end sections, and  $x_O$ ,  $x_A$ ,  $x_B$ ,  $x_C$ ,  $y_O$ ,  $y_A$ ,  $y_B$ , and  $y_C$  are the coordinates of points O, A, B, and C.

For the middle section, the deformation depends on the mutual position of points A, B, and the pre-deflection of the filament:

$$\Delta l_2 = \sqrt{(x_A - x_B)^2 + (y_A - y_B)^2} - l_{20} + 2\Delta l_{s0}(1 - \lambda_0). \quad (9)$$

The stiffness of the end sections is

$$k_l = \frac{E_1 A}{l_{01}}, \quad (10)$$

where  $A$  is the cross-sectional area, and the Young's modulus  $E_1$  is

$$E_1 = E_m, \quad (11)$$

where  $E_m$  is the NiTi module in the martensitic state. This is the case if it is assumed that the temperature in the final sections is lower than the final martensitic temperature, i.e.,  $T < M_f$ . The Young's modulus according to [31] is equal to the modulus of NiTi in the fully martensite state.

For the middle section, the stiffness is

$$k_T = \frac{E_{02} A}{l_{20}}, \quad (12)$$

where the Young's modulus  $E_{02}$  is defined by the piecewise function

$$E_2 = \begin{cases} E_a - (E_a - E_m)R_m & \text{if } 0 \leq \varepsilon_{s2} \leq \varepsilon_m^y \\ E_a - (E_a - E_T)R_m & \text{if } \varepsilon_m^y \leq \varepsilon_{s2} \leq \varepsilon_m^d \\ E_a - (E_a - E_d)R_m & \text{if } \varepsilon_m^d \leq \varepsilon_{s2} \end{cases}, \quad (13)$$

where  $E_m$ ,  $E_T$ ,  $E_d$ , and  $E_a$  are Young's modulus of the fully twined, partially twined, detwinned martensite, and austenite, respectively;  $\varepsilon_m^y$  is the yield strain of the twined martensite;  $\varepsilon_m^d$  is the minimum strain of the detwinned martensite; and

$$\varepsilon_{s2} = \frac{\Delta l_2}{l_{02}} = \frac{\sqrt{(x_A - x_B)^2 + (y_A - y_B)^2} - l_{20} + 2\Delta l_{s0}(1 - \lambda_0)}{l_{20}} \quad (14)$$

is the current strain of the middle section of the filament.

The relative martensitic fraction  $R_m$  of NiTi is calculated according to [31], and to investigate the major and minor hysteresis, similarly to [18], it is modified in the following form:

$$R_m = \frac{S_R}{2} \left( 1 + \tanh \frac{T_m - T}{\lambda_T} \right) + R_C S_R, \quad (15)$$

where  $S_R$  is a scale factor dependent on the temperature fluctuation,  $R_C$  is a factor dependent on where the temperature change point is located, and  $\lambda_T$  is a relative temperature dependent on the crystallographic transformation temperatures of the NiTi. The temperature  $T_m$  depends on whether the thermal process is heating or cooling and is obtained by the following relation:

$$T_m = \frac{1}{2} \begin{cases} A_s + A_f & \text{if } \frac{dT}{dt} > 0 \\ M_s + M_f & \text{if } \frac{dT}{dt} < 0 \end{cases}. \quad (16)$$

The coefficient  $\lambda_T$  has unit °C and, here, it has the following form:

$$\lambda_T = \frac{1}{2} \begin{cases} \frac{A_s + A_f - b_a}{c_a} & \text{if } \frac{dT}{dt} > 0 \\ \frac{M_s + M_f - b_m}{c_m} & \text{if } \frac{dT}{dt} < 0 \end{cases}, \quad (17)$$

and  $A_s$ ,  $A_f$ ,  $M_s$ , and  $M_f$  are the start and final temperatures for austenite and martensite of SMA. The limiting values of the coefficients,  $b_a < 0.5(A_f - A_s)$ ,  $b_m < 0.5(M_s - M_f)$ ,  $c_a < 0.5$ , and  $c_m < 0.5$  have been established experimentally [31].

The major and minor hystereses of the relative martensitic fraction are determined using the method described in [18], adapted for the model of [31]. In summary, this method is based on the points at which the temperature process changes from warming to cooling and vice versa. According to the adopted method, if the temperature gradient change point  $T_f$  is in the transition periods when both martensite and austenite fractions are present in the SMA, i.e.,

$$T_f \in [M_s, M_f] \cap [A_f, A_s], \quad (18)$$

the scale factor of the martensitic fraction acquires the values of the case of transition from heating to cooling, equivalent to

$$\dot{T}_{f-} > 0 \text{ and } \dot{T}_{f-} < 0, \quad (19)$$

where  $\dot{T}_{f-}$  and  $\dot{T}_{f-}$  are the temporal temperature gradients before and after the onset of the fluctuation, respectively. The scale factor of the martensitic fraction has the following form:

$$S_R = \begin{cases} 1 & \text{if } M_s > T_f > M_f \\ R_m^f = \frac{1}{2} \left( 1 + \tanh \frac{T_m - T_f}{\lambda_T} \right) & \text{if } A_f > T_f > A_s \end{cases}, \quad (20)$$

and the fraction

$$R_C = \begin{cases} 0 & \text{if } M_s > T_f > M_f \\ 0 & \text{if } A_f > T_f > A_s \end{cases}. \quad (21)$$

If, at the change point, the temperature changes from cooling to warming, then the following applies:

$$\dot{T}_{f-} < 0 \text{ and } \dot{T}_{f-} > 0. \quad (22)$$

The scale coefficients are, respectively,

$$S_R = \begin{cases} 1 - R_m^f & M_s > T_f > M_f \\ R_m^f = \frac{1}{2} \left( 1 + \tanh \frac{T_m - T_f}{\lambda_T} \right) & \text{if } M_s \geq T_f \geq M_f \end{cases} \quad (23)$$

and

$$R_C = \begin{cases} 0 & \text{if } M_f > T_f > A_f \\ 1 - R_m^f & \text{if } M_s > T_f > M_f \end{cases} \quad (24)$$

A sub minor hysteresis occurs if a minor hysteresis already exists after the point  $T_f$ . The temperature at which sub minor hysteresis occurs is denoted by  $T_f^s$ . The other important conditions for sub minor hysteresis existing are when cooling,  $M_f < T_f^s < M_s$ , and when warming,  $A_s < T_f^s < A_f$ .

For a sub minor hysteresis, the following scale factors are valid for the warming-to-cooling transition:

$$S_R = \begin{cases} 1 & \text{if } M_f > T_f^s > A_f \\ R_m^{fs} = \frac{1}{2} \left( 1 + \tanh \frac{T_m - T_f^s}{\lambda_T} \right) & \text{if } A_f > T_f^s > A_s \end{cases} \quad (25)$$

and

$$R_C = \begin{cases} 0 & \text{if } M_s > T_f^s > M_f \\ 0 & \text{if } A_f > T_f^s > A_s \end{cases} \quad (26)$$

At the transition from cooling to warming, the scale coefficients are

$$S_R = \begin{cases} R_m^f - R_m^{fs} & \text{if } M_f > T_f^s > A_f \\ R_m^{fs} = \frac{1}{2} \left( 1 + \tanh \frac{T_m - T_f^s}{\lambda_T} \right) & \text{if } M_s > T_f^s > M_f \end{cases} \quad (27)$$

and

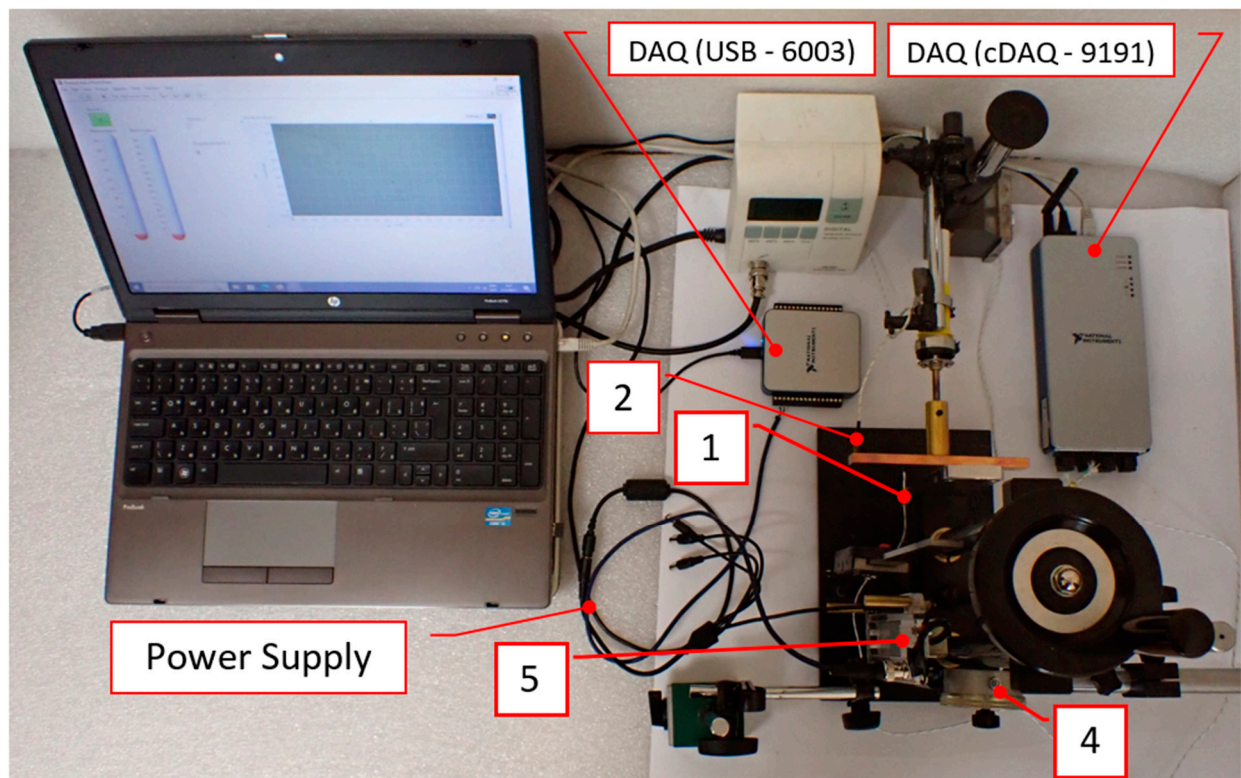
$$R_C = \begin{cases} 0 & \text{if } M_f > T_f^s > M_s \\ 1 - R_m^{fc} & \text{if } M_s > T_f^s > M_f \end{cases} \quad (28)$$

To determine the heater temperature distribution in the area where the SMA filament moves, the experimental setup shown in Figure 2 was designed. The temperature in the vicinity of the heater (3) was measured using a movable thermocouple (1), the position of which was set using an inductive position sensor (5) type APO-075-002-000 of TT Electronics Ltd., Woking, UK. The constant temperature of the heater is measured by a thermocouple (2) which is fixed in its body. A mechanical dial gauge (4) was also added to the experimental system to calibrate the data of the inductive sensor (5). The data from the two thermocouples are fed to a data acquisition system (DAQ) type cDAQ -9191, and the inductive sensor signal is fed into a DAQ type USB -9191 of National Instruments Ltd. The data are processed and recorded by a LabVIEW program. Different values of the constant temperature of the heater are set using a thermostat, and by changing the position of the movable thermocouple, the type of heat field in the vicinity of the heater is determined.

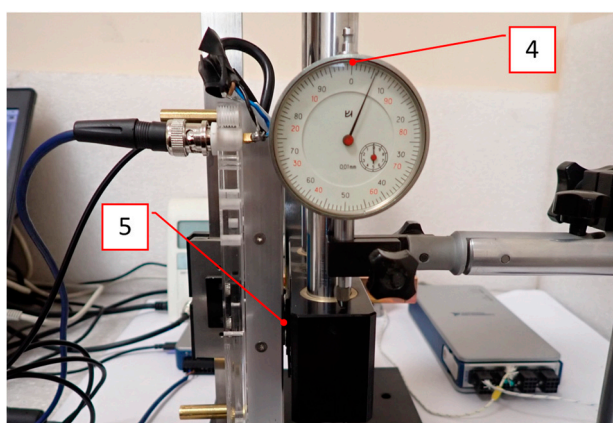
Based on the experiments, the temperature of the filament in the middle part is assumed to be a stationary function of the y coordinate defined by the piecewise function:

$$T = \begin{cases} (T_h - T_0)e^{-\left(\frac{y-y_e}{\theta}\right)^2} + T_0 & \text{if } y < y_e \\ T_h & \text{if } y_e \leq y \leq y_f \\ (T_h - T_0)e^{-\left(\frac{y-y_f}{\theta}\right)^2} + T_0 & \text{if } y > y_f \end{cases}, \quad (29)$$

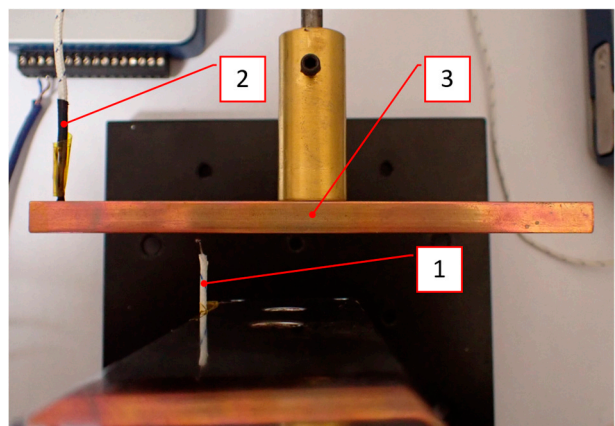
where  $y_e$ ,  $y_f$  are coordinates dependent on the heater position determined experimentally (Figure 3),  $T_h$  is the maximum temperature received by the filament from the heater,  $\theta$  is a conditional length defining the slope of the curve  $T = T(y)$ , and  $T_0$  is the room temperature.



(a)



(b)



(c)

Figure 2. Cont.

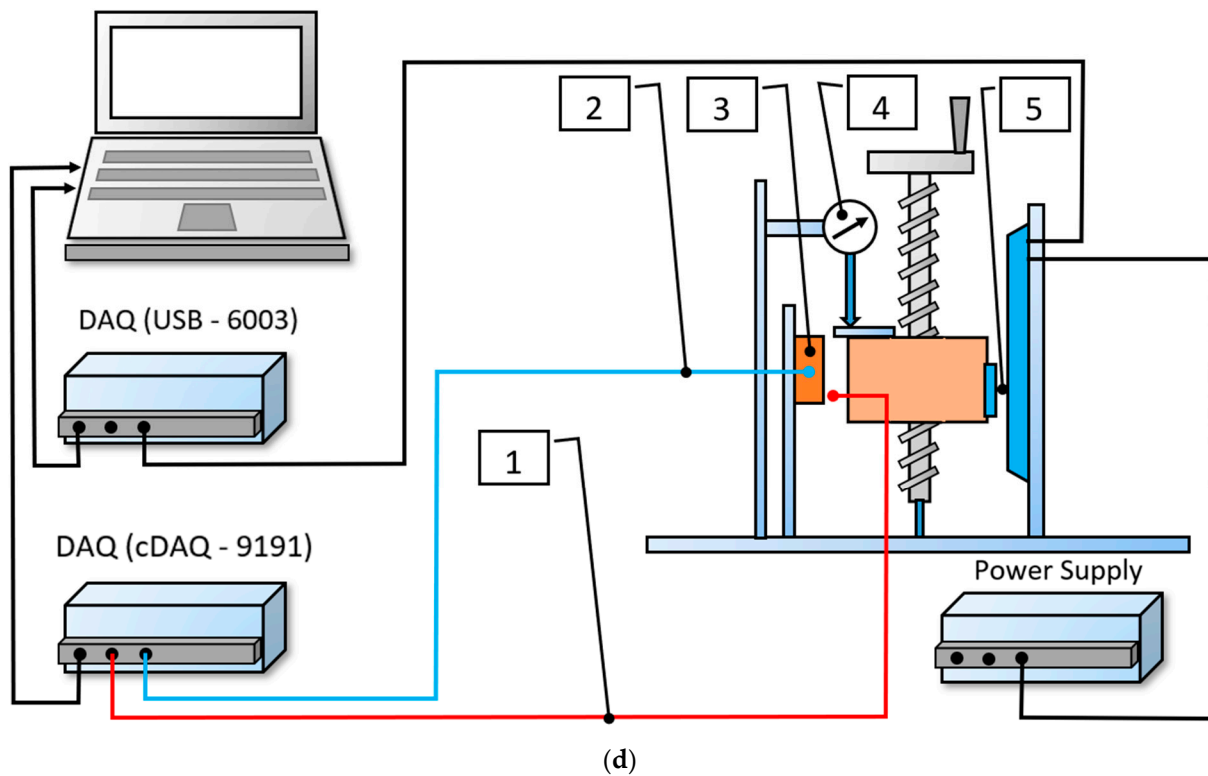


**Figure 2.** Experimental system for studying the heater’s thermal field: (a) top view photo; (b) close-view of the inductive position sensor (5) and the dial gauge (4); (c) close-view of the movable thermocouple (1), the thermocouple of the heater (2), and the heater (3); (d) block diagram. (1) Movable thermocouple; (2) heater thermocouple; (3) heater; (4) dial gauge; (5) inductive position sensor.

In Figure 3 the experimental values of the heater’s thermal field for three maximal temperatures—60, 67, and 78 °C—are presented with solid lines. The corresponding approximated thermal fields are presented with dashed lines.

The approximated heat field function along the vertical coordinate gives rise in this model to consideration of the relative martensitic fraction as a complex function of the  $y_A$  coordinate and time  $t$ , i.e.,

$$R_m = R_m(y_A(t)). \quad (30)$$

From this, it follows that the Young’s modulus and stiffness of the SMA filament in the middle section are considered, respectively, to be

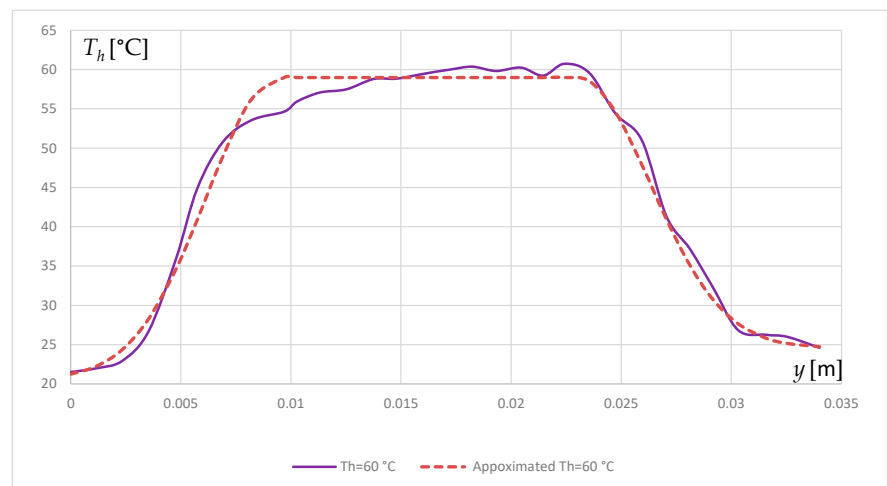
$$E_2 = E_2(x_A(t), y_A(t)), \quad (31)$$

and

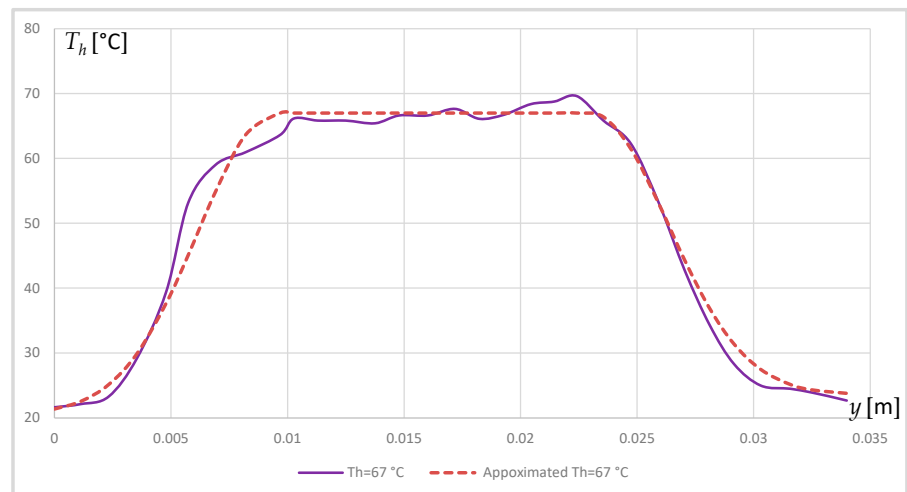
$$k_T = k_T(x_A(t), y_A(t)). \quad (32)$$

The assumption about the temperature dependence of the middle section on the  $y$  position leads to the representation of the thermal stiffness as a function of time. The potential character for the temperature distribution near the heater provides a rationale for deriving the filament forces from the SMA to be derived via the second-order Lagrange equations.

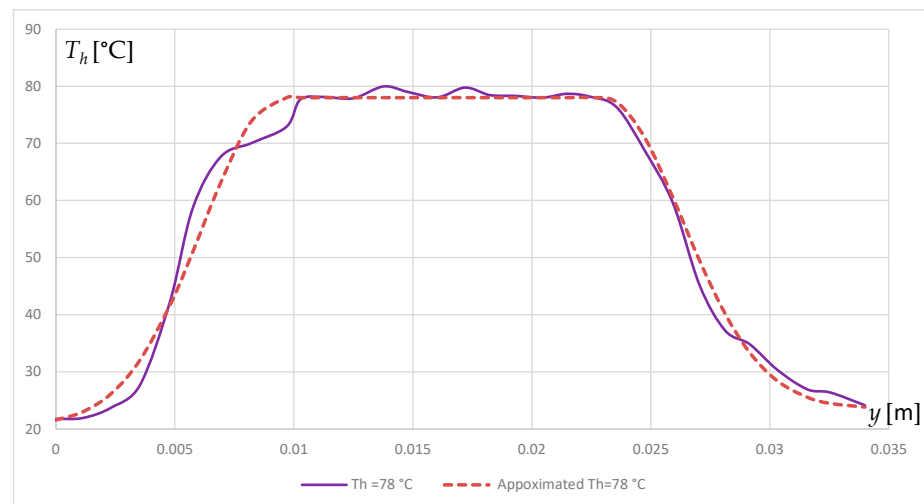
It is assumed that the motion of the filament is such that the oscillator is only in its symmetric configuration, where  $x_B = -x_A$ ,  $y_B = y_A$ ,  $x_O = -l$ ,  $x_C = l$ ,  $y_C = y_O = 0$ ,  $l_{30} = l_{10}$ ,  $\Delta l_3 = \Delta l_1$ , and  $l = OC/2$ .



(a)



(b)



(c)

**Figure 3.** Experimental and approximated SMA filament temperature distribution along the y coordinate: (a) for a heater temperature of 60 °C; (b) for a heater temperature of 67 °C; (c) for a heater temperature of 78 °C.

In this case, the Lagrangian of the oscillator takes the following form:

$$L = E_K - E_P = m(\dot{x}_A^2 + \dot{y}_A^2) - k_1 \Delta l_1^2 - 2k_T(x_A, y_A) \Delta l_{22}^2(y_A), \quad (33)$$

where the symmetry-transformed deformation of the middle section is rewritten as

$$\Delta l_2 = 2\Delta l_{22}(x_A). \quad (34)$$

Here,  $\Delta l_{22}(x_A)$  expresses the following:

$$\Delta l_{22}(x_A) = x_A - \frac{l_{20}}{2} + \Delta l_{s0}(1 - \lambda_0), \quad (35)$$

Which can be rewritten as

$$\Delta l_{22}(x_A) = x_A + l_{22}, \quad l_{22} = -\frac{l_{20}}{2} + \Delta l_{s0}(1 - \lambda_0). \quad (36)$$

The strain of the middle segment is expressed as

$$\varepsilon_{s2} = \frac{2(x_A + l_{22})}{l_{20}}, \quad (37)$$

and the deformation of the end section is converted into the following:

$$\Delta l_1 = \sqrt{(x_A + l)^2 + y_A^2} - l_{10} + \Delta l_{s0}\lambda_0. \quad (38)$$

In the above formula, the expression  $-l_{10} + \Delta l_{s0}\lambda_0$  is denoted as  $l_{11}$ , and the deformation of second section obtains the following form:

$$\Delta l_1 = \sqrt{(x_A + l)^2 + y_A^2} + l_{11}. \quad (39)$$

The differentiation of the Lagrangian is performed with respect to the generalized coordinates  $x_A$  and  $y_A$  and the generalized velocities  $\dot{x}_A$  and  $\dot{y}_A$ , according to the Lagrange equations of the second kind:

$$\frac{d}{dt} \frac{\partial L}{\partial \dot{q}_i} - \frac{\partial L}{\partial q_i} = Q_i \quad i = 1, 2, \quad (40)$$

where  $\{q_1, q_2\} = \{x_A, y_A\}$ ,  $\{\dot{q}_1, \dot{q}_2\} = \{\dot{x}_A, \dot{y}_A\}$ , and  $\{Q_1, Q_2\} = \{-\beta_x \dot{x}, -2mg - \beta_y \dot{y}\}$  are the generalized coordinate, generalized velocity, and generalized force, respectively, and are the damping coefficients along the  $x$  and  $y$  axes.

After differentiation according to (40) the system of differential equations is derived:

$$\begin{cases} m\ddot{x} + k_1 \Delta l_1(x) \frac{d\Delta l_1(x, y)}{dx} + \frac{\partial k_T(x, y)}{\partial x} \Delta l_{22}(x)^2 + 2k_T(x, y) \Delta l_{22}(x) \frac{d\Delta l_{22}(x)}{dx} = -\beta_x \dot{x} \\ m\ddot{y} + \frac{\partial k_T(x, y)}{\partial y} \Delta l_{22}(x)^2 - k_1 \Delta l_1(x) \frac{d\Delta l_1(x, y)}{dy} + \frac{\partial k_T(x, y)}{\partial y} \Delta l_{22}(x)^2 = -mg - \beta_y \dot{y} \end{cases}, \quad (41)$$

where the derivative of the filament end segment with respect to  $x$  is

$$\frac{d\Delta l_1(x)}{dx} = \frac{x + l}{\sqrt{(x + l)^2 + y^2}}. \quad (42)$$

The derivative of the middle filament segment with respect to  $x$  is

$$\frac{d\Delta l_{22}(x)}{dx} = 1. \quad (43)$$

The stiffness  $k_T$  does not depend on  $x$ , and its derivative with respect to  $x$  is equal to zero, or

$$\frac{\partial k_T(x, y)}{\partial x} = 0. \tag{44}$$

The derivative of  $k_T$  with respect to  $y$  is equal to

$$\frac{\partial k_T(x, y)}{\partial y} = \frac{\partial E_{02}A}{\partial y l_{02}} = \frac{A}{l_{02}} \frac{\partial E_{02}}{\partial y}. \tag{45}$$

In (41), the partial derivative of Young’s modulus with respect to  $y$  for the middle section has the following form:

$$\frac{\partial E_2}{\partial y} = \begin{cases} (E_m - E_a) \frac{dR_m}{dy} & \text{if } 0 \leq \varepsilon_{s2} \leq \varepsilon_m^y \\ (E_T - E_a) \frac{dR_m}{dy} & \text{if } \varepsilon_m^y \leq \varepsilon_{s2} \leq \varepsilon_m^d \\ (E_d - E_a) \frac{dR_m}{dy} & \text{if } \varepsilon_m^d \leq \varepsilon_{s2} \end{cases} . \tag{46}$$

The relative martensite fraction, taking into account the heater heat field distribution function (29), is modified into

$$R_m = \begin{cases} \frac{S_R}{2} \left( 1 - \tanh \frac{T_m - T_h e^{-\frac{1}{\theta^2}(y-y_e)} + T_0}{\lambda_T} \right) + R_C S_R & \text{if } y \leq y_e \\ \frac{S_R}{2} \left( 1 - \tanh \frac{T_m - T_h + T_0}{\lambda_T} \right) + R_C S_R & \text{if } y_e < y < y_f \\ \frac{S_R}{2} \left( 1 - \tanh \frac{T_m - T_h e^{-\frac{1}{\theta^2}(y-y_f)} + T_0}{\lambda_T} \right) + R_C S_R & \text{if } y \geq y_f \end{cases} . \tag{47}$$

The derivative of the relative martensite fraction in this case is

$$\frac{dR_m}{dy} = \begin{cases} \frac{S_R T_h}{2\lambda_T \theta^2} e^{-\frac{1}{\theta^2}(y-y_e)} \left( 1 - \tanh \frac{T_m - T_h e^{-\frac{1}{\theta^2}(y-y_e)} + T_0}{\lambda_T} \right) & \text{if } y \leq y_e \\ 0 & \text{if } y_e < y < y_f \\ \frac{S_R T_h}{2\lambda_T \theta^2} e^{-\frac{1}{\theta^2}(y-y_f)} \left( 1 - \tanh \frac{T_m - T_h e^{-\frac{1}{\theta^2}(y-y_f)} + T_0}{\lambda_T} \right) & \text{if } y > y_f \end{cases} . \tag{48}$$

After the simplifications described above, the dynamic model (41) is recast into a system of differential equations:

$$\begin{cases} m\ddot{x} + \frac{E_m A(x+l) \left( \sqrt{(x+l)^2 + y} - l_{11} \right)}{l_{10} \sqrt{(x+l)^2 + y}} + 2k_T(x, y)(x+l_{22}) = -\beta_x \dot{x} \\ m\ddot{y} + \frac{\partial k_T(x, y)}{\partial y} (x+l_{22})^2 + \frac{E_m A \left( \sqrt{(x+l)^2 + y} - l_{11} \right) y}{l_{10} \sqrt{(x+l)^2 + y}} = -mg - \beta_y \dot{y} \end{cases} . \tag{49}$$

In order to find a numerical solution of the system (49), its order is lowered by the following substitutions:

$$\begin{cases}
 \dot{v}_x = -\frac{E_m A (x+l) \left( \sqrt{(x+l)^2 + y} - l_{11} \right)}{m l_{01} \sqrt{(x+l)^2 + y}} - \frac{2}{m} k_T(x,y) (x+l_{22}) - \frac{\beta_x}{2m} \dot{x} \\
 \dot{x} = v_x \\
 \dot{v}_y = \frac{E_m A \left( \sqrt{(x-l)^2 + y} - l_{11} \right) y}{m l_{10} \sqrt{(x-l)^2 + y}} - \frac{\partial k_T(x,y)}{m \partial y} (x+l_{22})^2 - g - \frac{\beta_y}{2m} \dot{y} \\
 \dot{y} = v_y
 \end{cases} \quad (50)$$

The numerical solution of the system was carried out using the parameters given in Table 1.

**Table 1.** Values of the parameters of the system of differential equations.

Parameter	Symbol	Value	Unit
Half-support distance	$l$	0.026	m
NiTi filament half length	$l_s$	0.25	m
Mass of a sphere	$m$	0.012	kg
Gravity acceleration	$g$	9.81	m/s <sup>2</sup>
Lengths of NiTi filament end sections	$l_{10} = O A_0 l_{30} = B_0 C$	0.14	m
Length of the middle section of the NiTi filament	$l_{20} = A_0 B_0$	0.24	m
Diameter of NiTi filament	$ds$	0.00025	m
Young's modulus for NiTi in fully twinned martensite *	$E_m$	21.7	GPa
Young's modulus for NiTi in partially twinned martensite *	$E_T$	0.56	GPa
Young's modulus for NiTi in detwinned martensite *	$E_d$	11.1	Gpa
Young's modulus for NiTi in austenite *	$E_a$	55.5	Gpa
Yield strain for twinned NiTi in martensite *	$\varepsilon_m^y$	0.0024	
Minimum strain of twinned NiTi in martensite *	$\varepsilon_m^d$	0.0044	
Starting austenite temperature of NiTi *	$A_S$	55.99	°C
Final austenite temperature of NiTi *	$A_f$	64.05	°C
Starting martensitic temperature of NiTi *	$M_s$	25.4	°C
Final martensitic temperature of NiTi *	$M_f$	21.44	°C
Austenite correction temperature	$b_a$	0.01	°C
Austenite coefficient	$c_a$	1.95	
Martensitic correction temperature	$b_m$	0.01	°C
Martensitic coefficient	$c_m$	2.17	
Start position of maximum temperature	$y_e$	0.0095	m
End position of maximum temperature	$y_f$	0.023	m
Room temperature	$T_0$	20	°C
Maximum temperature of NiTi filament	$T_h$	70	°C
Longitudinal damping coefficient	$\beta_x$	0.00042	kg/s
Transverse damping coefficient	$\beta_y$	0.0014	kg/s

\* The NiTi properties in Table 1 were obtained from experimental data published in [35].

To solve the system (50), a numerical solution program was created using an implicit fifth-order Euler method. The solutions of the system of differential Equation (50) were obtained under zero initial conditions for the velocities  $\dot{x}$  and  $\dot{y}$ , and the initial conditions for the coordinates of the masses were taken as  $x(0) = -0.1$  and  $y(0) = 0.01$ .

#### 4. Conducting the Experiments and Comparing the Results

The displacements of the spheres along the  $x$  and  $y$  coordinates were measured synchronously in real time using the experimental system shown in Figure 4. A photograph of the system is shown in Figure 4a, and its simplified block diagram is depicted in Figure 4b. Filament 1 is immovably clamped on two supports (6). Two spheres (4) are arranged symmetrically with respect to the heater (3) and the fixed supports. On the filament adjacent to the spheres, movable sensing elements of non-contact inductive sensors (2) and (5) are mounted, which are type APO-075-002-000 of TT Electronics Ltd., UK. In order to detect the simultaneous displacement of the spheres in the horizontal  $x$ -direction and the vertical  $y$ -direction, the movable sensing elements and the sensor bodies are oriented at 90 degrees to each other. In Figure 4, sensor (2) measures the  $x$ -axis sphere displacement, and sensor (5) is oriented to measure the vertical  $y$ -displacement of the sphere. The signals from the two sensors are input to the data acquisition system DAQ USB-6003 from National Instruments then processed by a laptop using a LabVIEW program. The data from both sensors and the heater temperature are recorded in an Excel file.

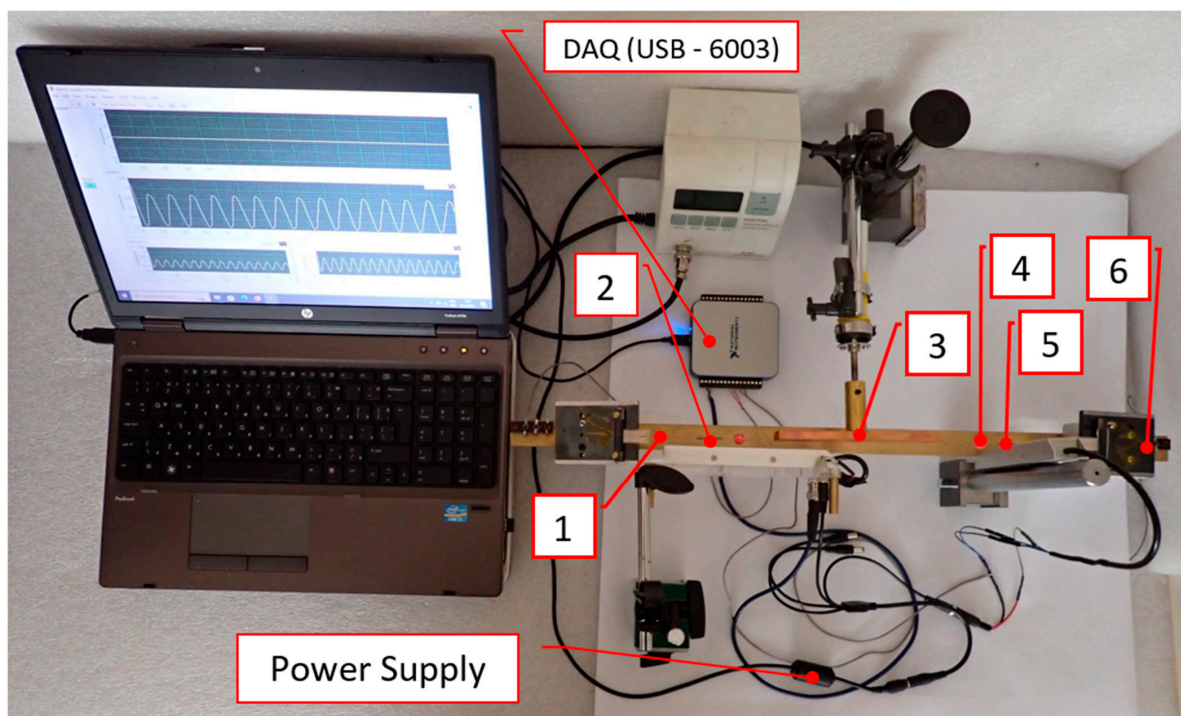
Multiple experiments were conducted by varying the weights masses, the initial tension of the SMA filament, and the heater temperature, which was kept constant using a thermoregulator.

In the experiments, it was found that for oscillations to occur, certain conditions concerning the pre-tension of the SMA filament and the difference in room and heater temperature needed to be met. The most significant influence for the occurrence of oscillations is the initial position of the filament relative to the heater. Once the conditions for the oscillations to occur are satisfied, stable oscillations of the filament with both masses are generally observed with unchanging energy (Supplementary Materials).

Analysis of the experimental results shows that the self-excited oscillations have a stochastic character. The reason for the appearance of the random processes is due to the nonlinear hysteresis variations of the Young's modulus of the SMA, which are a function of the temperature, the sign of its gradient, the type of deformation, and the position of the SMA filament.

Figure 5a shows the plot of the experimental measurements of the  $x$ -axis position of the sphere. It can be seen that the oscillatory motion has a period which varies randomly within certain limits, while the amplitude also varies according to a random distribution law.

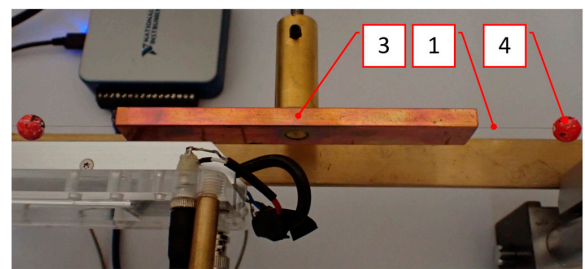
An interesting impression of the  $x$ -axis oscillations is an extra modulated oscillation with approximately 20 times the frequency and approximately 5 times the amplitude. This modulation is also confirmed in Figure 5b, which represents the result of the theoretical model for the  $x$ -axis oscillations. The logical explanation for this phenomenon, according to the authors, is the existence of a purely mechanical normal vibration of the SMA filament that occurs under the action of the variable axial force. This variable axial force is generated by the thermal contractions of the SMA filament. The difference in the frequencies of the two oscillations is due to the fact that the mechanical oscillations have a frequency which depends on the stiffness of the filament and mass, while the thermal oscillations depend on the vertical position of the filament and primarily on the temperature and time constant of the filament determining the heating cooling time. For the same reasons, the amplitudes of the longitudinal mechanical oscillations have a small value, while the thermal amplitudes can reach up to 8% of the filament length. Thus, the  $x$ -axis displacement can be assumed to be the sum of mechanical and thermal random oscillatory motions.



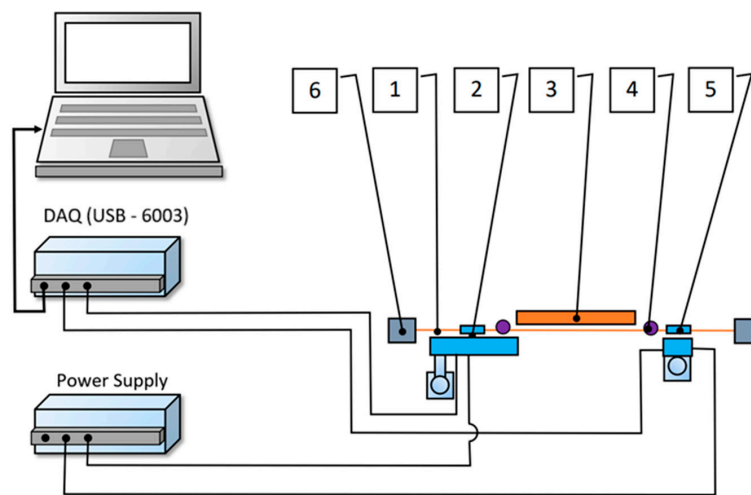
(a)



(b)

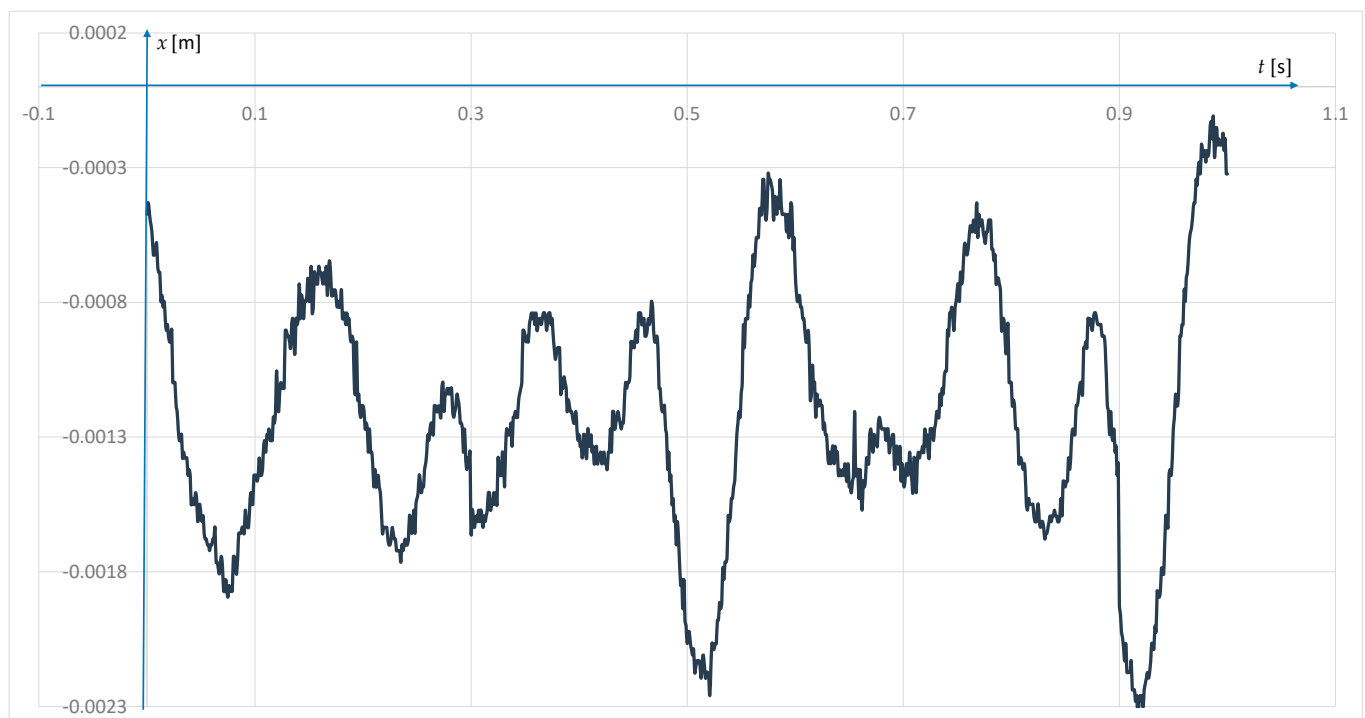


(c)

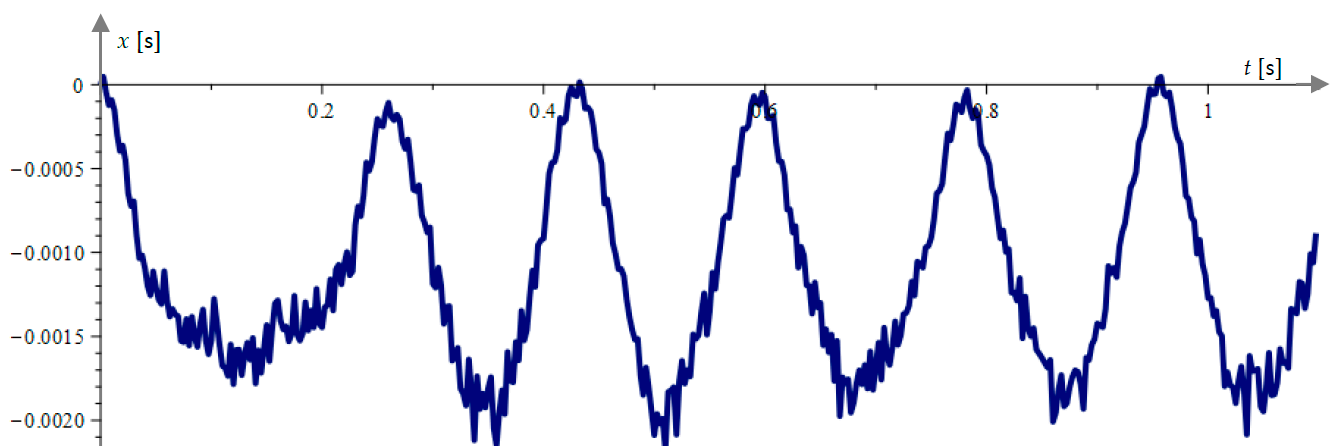


(d)

**Figure 4.** Experimental system for measuring the displacements of spheres in two perpendicular directions: (a) top view; (b) close-view of the inductive sensor 2 for x-position, and the inductive sensor 5 for y position; (c) close-view of the SMA filament (1), the heater (3), and the two masses (4); (d) block diagram. (1) SMA filament; (2) inductive x-axis position sensor; (3) heater; (4) sphere; (5) inductive y-axis position sensor; (6) support.



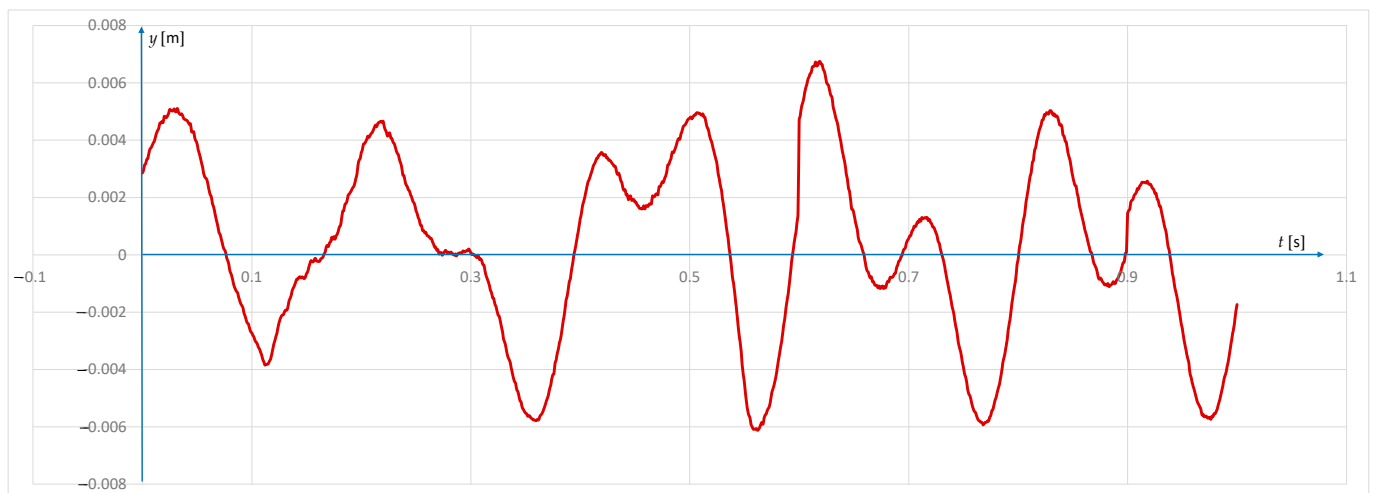
(a)



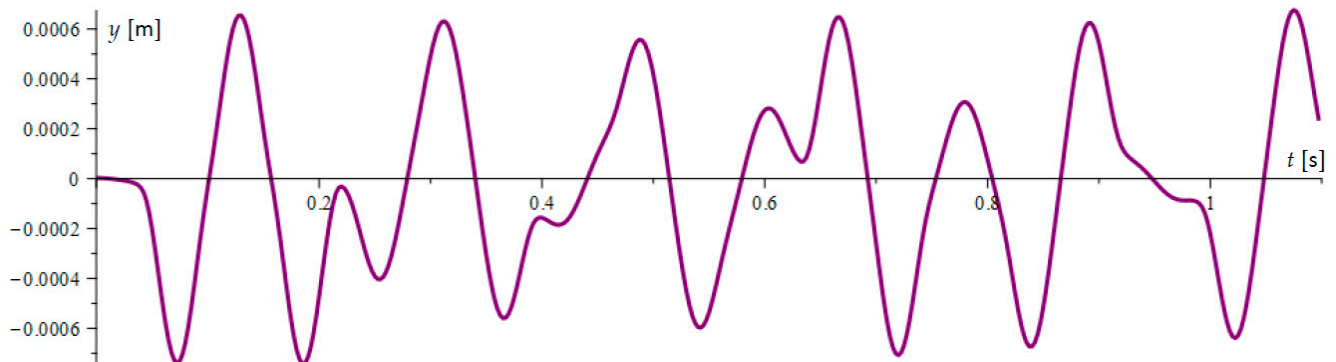
(b)

**Figure 5.** Oscillations along the  $x$ -axis at sphere masses of 0.012 kg, a 5% pre-stretch, and a heater temperature of 80 °C: (a) experimental data; (b) dynamic model data.

Figure 6 plots the displacements of the sphere along the  $y$ -axis. The experimental data are shown in Figure 6a, and the data obtained from the dynamic model are plotted in Figure 6b. It can be observed that stochasticity is also present in the vertical oscillations both in terms of period and frequency. Modulated oscillations along the  $y$ -axis direction are not seen in either the experimental data or the data obtained from the theoretical model. The reason for this is that here, the transverse oscillations are purely mechanical, induced by thermal contractions along the  $x$ -axis. The appearance of the stochasticity here is also explained by the change in Young's modulus at different temperatures and strains.



(a)



(b)

**Figure 6.** Oscillations along the  $y$ -axis for sphere masses of 0.012 kg, a pre-stretch of 5%, and a heater temperature of 80 °C: (a) experimental data; (b) dynamic model data.

## 5. Conclusions

A new system for self-excited thermomechanical oscillations based on shape memory alloys was created. The properties of this system are investigated theoretically by a dynamic model in which the hysteresis properties of the SMA are accounted for. The results obtained from the model are confirmed by direct measurements of displacements along two perpendicular directions. Using this experimental method, displacements were obtained with relatively high accuracy since integration errors typical of inertial measurement systems such as MEMS accelerometers or gyroscopes were eliminated. The obtained results show that the oscillations of the system have a stochastic character in terms of frequency and vibration. It is found that due to the birefringent nature of the oscillations along the  $x$ -axis, there are two types of oscillations. The main ones, called thermal, have an amplitude dependent on the thermal contractions of the filament and a frequency determined by the temperature time constant of the filament from the SMA. The second oscillations, called purely mechanical, have a frequency dependent on the ratio of the mass of the sphere and the stiffness of the system and an amplitude that is a function of the longitudinal thermal contractions, the natural frequency, and the damping of the SMA filament.

**Supplementary Materials:** The following supporting information can be downloaded at: <https://www.mdpi.com/article/10.3390/act13050182/s1>, Video S1: Oscillations of the sensing element of the inductive sensor.

**Author Contributions:** Conceptualization, T.T. and G.T.; methodology, T.T.; software, T.T.; validation, I.Y.; formal analysis, G.T.; investigation, T.T.; resources, T.T. and I.Y.; writing—original draft preparation, T.T.; writing—review and editing, G.T. and I.Y.; supervision, G.T.; project administration, G.T.; funding acquisition, G.T. All authors have read and agreed to the published version of the manuscript.

**Funding:** This research was funded by the European Union—NextGenerationEU through the National Recovery and Resilience Plan of the Republic of Bulgaria, project № BG-RRP-2.004-0005.

**Data Availability Statement:** Data are contained within the article.

**Conflicts of Interest:** The authors declare no conflicts of interest.

## References

- Kroger, M.; Neubaer, M.; Popp, K. Experimental investigation on the avoidance of self-excited vibrations. *Philos. Trans. R. Soc. A* **2008**, *366*, 785–810. [[CrossRef](#)] [[PubMed](#)]
- Ding, W. Modeling and Control. In *Self-Excited Vibration*; Springer: Berlin/Heidelberg, Germany, 2010. [[CrossRef](#)]
- Papangelo, A.; Putignano, C.; Hoffmann, N. Self-excited vibrations due to viscoelastic interactions. *Mech. Syst. Signal Process.* **2020**, *144*, 106894. [[CrossRef](#)]
- Nesis, E.I.; Nesis, S.E. Thermomechanical and thermoacoustic self-excited oscillations. *J. Eng. Phys.* **1988**, *55*, 1178–1194. [[CrossRef](#)]
- Khvol'son, O.D. *Physics Course*; Nabu Press: Berlin, Germany, 1923; Volume 3.
- Awrejcewicz, J.; Pyryev, Y. Thermo-mechanical model of frictional self-excited vibrations. *Int. J. Mech. Sci.* **2005**, *47*, 1393–1408. [[CrossRef](#)]
- Astashev, V.K.; Korendyasev, G.K. Thermomechanical model of the occurrence of oscillations in metal cutting. *J. Mach. Manuf. Reliab.* **2012**, *41*, 189–193. [[CrossRef](#)]
- Fel'dshtein, V.A. Thermomechanical Self-Excited Oscillations of Current-Carrying Conductors. *J. Appl. Mech. Tech. Phys.* **2017**, *58*, 1091–1098. [[CrossRef](#)]
- Toda, A.; Tomita, C.; Hikosaka, M.; Hibno, Y.; Miyayji, H.; Nonomura, C.; Suzuki, T.; Ishihara, H. Thermo-mechanical coupling and self-excited oscillation in the neck propagation of PET films. *Polymer* **2002**, *43*, 947–951. [[CrossRef](#)]
- Weng, W.; Anstie, J.D.; Abbott, P.; Fan, B.; Stace, T.M.; Luiten, A.N. Stabilization of a dynamically unstable opto-thermo-mechanical oscillator. *Phys. Rev. A* **2015**, *91*, 063801. [[CrossRef](#)]
- Blocher, D.; Rand, R.H.; Zehnder, A.T. Analysis of laser power threshold for self oscillation in thermo-optically excited doubly supported MEMS beams. *Int. J. Non Linear Mech.* **2013**, *57*, 10–15. [[CrossRef](#)]
- Pandey, M.; Aubin, K.; Zalalutdinov, M.R.; Reichenbach, B.A.; Zehnder, T.; Richard, R.H.; Craighead, H.G. Analysis of Frequency Locking in Optically Driven MEMS Resonators. *J. Microelectromech. Syst.* **2006**, *15*, 1546–1554. [[CrossRef](#)]
- Pandey, M.; Rand, R.H.; Zehnder, A.T. Frequency Locking in a Forced Mathieu-van der Pol-Duffing System. *Nonlinear Dyn.* **2008**, *54*, 3–12. [[CrossRef](#)]
- Wei, L.; Kuai, X.; Bao, Y.; Wei, J.; Yang, L.; Song, P.; Zhang, M.; Yang, F.; Wang, X. The Recent Progress of MEMS/NEMS Resonators. *Micromachines* **2021**, *12*, 724. [[CrossRef](#)] [[PubMed](#)]
- Miller, J.M.L.; Shin, D.D.; Kwon, H.-K.; Shaw, W.S.; Kenny, T.W. Spectral narrowing of parametrically pumped thermomechanical noise. *Appl. Phys. Lett.* **2020**, *117*, 033504. [[CrossRef](#)]
- Chen, C.-Y.; Li, M.-H.; Li, S.-S. CMOS-MEMS Resonators and Oscillators: A Review. *Sens. Mater.* **2018**, *30*, 733–756. [[CrossRef](#)]
- Pillai, G.; Li, S.-S. Piezoelectric MEMS Resonators: A Review. *IEEE Sens. J.* **2021**, *21*, 12589–12605. [[CrossRef](#)]
- Mitrev, R.; Todorov, T.; Fursov, A.; Ganey, B. Theoretical and Experimental Study of a Thermo-Mechanical Model of a Shape Memory Alloy Actuator Considering Minor Hystereses. *Crystals* **2021**, *11*, cryst11091120. [[CrossRef](#)]
- Elahinia, M.H. *Shape Memory Alloy Actuators: Design, Fabrication, and Experimental Evaluation*; John Wiley & Sons, Ltd.: Toledo, Spain, 2016; p. 621. [[CrossRef](#)]
- Sohn, J.W.; Ruth, S.J.; Yuk, D.-G.; Choi, S.-B. Application of Shape Memory Alloy Actuators to Vibration and Motion Control of Structural Systems: A Review. *Appl. Sci.* **2023**, *13*, 995. [[CrossRef](#)]
- Todorov, T.; Mitrev, R.; Yatchev, I.; Fursov, A.; Ilin, A.; Fomichev, V. A Parametric Study of an Electrothermal Oscillator Based on Shape Memory Alloys. In Proceedings of the 21st International Symposium on Electrical Apparatus and Technologies (SIELA), Bourgas, Bulgaria, 3–6 June 2020; pp. 1–4. [[CrossRef](#)]
- Wang, L.; Melnik, R. Nonlinear dynamics of shape memory alloy oscillators in tuning structural vibration frequencies. *Mechatronics* **2012**, *22*, 1085–1096. [[CrossRef](#)]
- Mitrev, R.; Atamas, E.; Goncharov, O.; Todorov, T.; Iatcheva, I. Modeling and study of a novel electrothermal oscillator based on shape memory alloys. In Proceedings of the 9th International Scientific Conference “Techsys 2020”—Engineering, Technologies and Systems, Plovdiv, Bulgaria, 14–16 May 2020; Volume 878, p. 012059. [[CrossRef](#)]
- Rusinek, R.; Rekas, J. Modelling of shape memory alloy oscillator and its application to middle ear structural reconstruction. In Proceedings of the 22nd International Conference on Computer Methods in Mechanics, AIP Conference Proceedings, Lublin, Poland, 13–16 September 2018; Volume 1922, p. 100017. [[CrossRef](#)]

25. Kumari, N.; Rakotondrabe, M. Design and Development of a Lead-Free-Piezoelectric Energy Harvester for Wideband, Low Frequency, and Low Amplitude Vibrations. *Micromachines* **2021**, *12*, 1537. [[CrossRef](#)]
26. Yang, F.; Shi, Y.; Liu, J.; Wang, Z.; Tian, X. Design and Experimental Study of Shape Memory Alloy and Piezoelectric Composite Power Generation Device. *Micromachines* **2023**, *14*, 1434. [[CrossRef](#)]
27. Wang, X.; Qin, Q.; Lu, Y.; Mi, Y.; Meng, J.; Zhao, Z.; Wu, H.; Cao, X.; Wang, N. Smart Triboelectric Nanogenerators Based on Stimulus-Response Materials: From Intelligent Applications to Self-Powered Systems. *Nanomaterials* **2023**, *13*, 1316. [[CrossRef](#)] [[PubMed](#)]
28. Namli, O.; Taya, M. Design of piezo-SMA composite for thermal energy harvester under fluctuating temperature. *J. Appl. Mech.* **2011**, *78*, 031001. [[CrossRef](#)]
29. Todorov, T.S.; Fursov, A.S.; Mitrev, R.P.; Fomichev, V.V.; Valtchev, S.S.; Il'in, A.V. Energy Harvesting with Thermally Induced Vibrations in Shape Memory Alloys by a Constant Temperature Heater. *IEEE/ASME Trans. Mechatron.* **2022**, *27*, 475–484. [[CrossRef](#)]
30. Reddy, A.R.; Umapathy, M.; Ezhilaras, D.I.; Uma, G. Piezoelectric energy harvester with shape memory alloy actuator using solar energy. *IEEE Trans. Sustain. Energy* **2015**, *6*, 409–415. [[CrossRef](#)]
31. Mitrev, R.; Todorov, T.; Fursov, A.; Fomichev, V.; Il'in, A. A Case Study of Combined Application of Smart Materials in a Thermal Energy Harvester with Vibrating Action. *J. Appl. Comput. Mech.* **2021**, *7*, 372–381. [[CrossRef](#)]
32. Fursov, A.S.; Todorov, T.S.; Krylov, P.A.; Mitrev, R.P. On the Existence of Oscillatory Modes in a Nonlinear System with Hystereses. *Differ. Equ.* **2020**, *56*, 1081–1099. [[CrossRef](#)]
33. Chattaraj, N. Experimental Investigation and Empirical Analysis of a Shape-Memory-Alloy-Actuated Electromechanical Oscillator. *J. Vib. Eng. Technol.* **2022**, *10*, 741–750. [[CrossRef](#)]
34. Boschetto, A.; Bottini, L.; Costanza, G.; Tata, M.E. Shape Memory Activated Self-Deployable Solar Sails: Small-Scale Prototypes Manufacturing and Planarity Analysis by 3D Laser Scanner. *Actuators* **2019**, *8*, 38. [[CrossRef](#)]
35. Mitrev, R.; Todorov, T. A Case Study of Experimental Evaluation of the Parameters of Shape Memory Alloy Wires. In Proceedings of the TechSys 2021—Engineering, Technologies and Systems, AIP Conference Proceedings, Plovdiv, Bulgaria, 27–29 May 2021; Volume 2449. [[CrossRef](#)]

**Disclaimer/Publisher's Note:** The statements, opinions and data contained in all publications are solely those of the individual author(s) and contributor(s) and not of MDPI and/or the editor(s). MDPI and/or the editor(s) disclaim responsibility for any injury to people or property resulting from any ideas, methods, instructions or products referred to in the content.